Simulating Quadrupolar NMR Dynamics in Solid Electrolyte $Li_{10}GeP_2S_{12}$

Tabea Huss,[1, a)] Federico Civaia,[1, a)] Simone S. Köcher*,[2, 1] Karsten Reuter,[1] Josef Granwehr,[2, 3] and Christoph Scheurer[1, 2]

[1)] *Fritz-Haber Institute of the Max Planck Society, Berlin (DE)*

[2)] *Institute of Energy Technologies (IET-1), Forschungszentrum Jülich GmbH, Jülich (DE)*

[3)] *Institute of Technical and Macromolecular Chemistry, RWTH Aachen University, Aachen (DE)*

(*Electronic mail: s.koecher@fz-juelich.de)

(Dated: 24 October 2025)

Quadrupolar solid-state (SS) nuclear magnetic resonance (NMR) spectroscopy is an excellent tool to trace lithium (Li) ion diffusion in solid electrolytes due to its sensitivity to dynamics over timescales from nanoseconds to seconds. However, the structural and dynamical complexity of battery materials limits the unambiguous interpretation of experimental data. Fast ionic motion can partially average experimentally observable quantities, leaving the underlying distribution of electric field gradients (EFGs) experimentally inaccessible and thus the measured data hard to interpret. In contrast, atomic simulation approaches, while providing the structure–observable relationship, are often constrained to idealized models. Established methods such as density functional theory (DFT) remain computationally expensive for realistic time and length scales.

Here, we show how experimental complexity in the fast-ion conductor $Li_{10}GeP_2S_{12}$ (LGPS) can be approached via a machine-learning (ML) assisted workflow. ML acceleration enables microsecond-scale molecular dynamics (MD) simulations and efficient predictions of EFG tensors via a tensorial model. By time averaging the EFG tensors from the MD trajectory, we compute the temperature dependence of ^{7}Li NMR quadrupolar observables subject to motional narrowing. Our prediction of the quadrupolar coupling of 24 kHz for tetragonal LGPS is in excellent agreement with the experimental value of 23 kHz. Furthermore, we emulate a spin-alignment echo (SAE) experiment *in silico* and apply the inverse Laplace transform (ILT) to extract correlation times for ionic motion of Li in different LGPS crystal structures. Finally, we assess whether SAE can differentiate inter-grain versus intra-grain ion dynamics via the orientational dependence of the EFG tensor.

I. INTRODUCTION

Nuclear magnetic resonance (NMR) spectroscopy offers a wide range of noninvasive techniques to probe local atomic structure and dynamics in solids across a large range of timescales. For quadrupolar nuclei such as ^{7}Li ($S = 3/2$), the local chemical environment and dynamics may be accessed via their interaction with the local electric field gradient (EFG). The environment is probed by extracting the quadrupolar coupling from spectral measurements, whereas the dynamics can be probed by the spin alignment echo (SAE) experiment, which is widely used for its sensitivity to slow ionic motion on timescales of ~ 10 µs to seconds.[1–11] SAE probes ion dynamics via its sensitivity to changes in the local chemical environment, which is reflected in the on-site EFG. During diffusion, ions hop among spectroscopically nonequivalent sites, producing an echo decay that can be monitored experimentally. This decay arises from the loss of correlation of the quadrupolar frequency ω_Q, which is directly linked to the EFG seen by the hopping ion and to the quadrupolar frequency of its initial site.[12]

In parallel to experiment, computational NMR methods are increasingly being used to aid the interpretation of NMR experiments by the study of representative model systems. These methods have been widely employed to compute NMR quadrupolar observables, traditionally by computing the EFG tensor via *ab initio* calculation such as density functional theory (DFT).[9,13–15] However, these approaches are computationally expensive, and thus limit the size of studied model systems and the accessible timescale. Recent advances have attempted to address this shortcoming by introducing the use of surrogate machine–learning (ML) models, that are faster while retaining the *ab initio* accuracy.[16–20] Model architectures using graph neural networks and Gaussian process regression have shown the capability of predicting with high accuracy and the importance of learning the symmetry of the tensor has been highlighted.[16,17] These advances in the field have enabled understanding when temperature effects are non-negligible[13] and incorporate them when needed.[16,17,19,21]

In the context of simulated SAE experiment, Harper *et al.* have coupled ML interatomic potentials with ML tensorial models to compute the quadrupolar frequency autocorrelation function (ACF) to emulate experimental echo decay in the ionic conductor Li_3PS_4 (LPS).[22] While this work has set a cornerstone for computational SAE, several factors remained unaddressed. First, no direct comparison to experiment was possible as no quadrupolar experiments on LPS are available in the literature. Secondly, the correlation time has been extracted by single-exponential fitting, which severely limited the recoverable kinetic information. In contrast, experimental analyses employing inversion techniques as inverse Laplace transform (ILT) have been demonstrated to be better suited to resolve multiple correlation times.[23] Lastly, this approach has been limited to the bulk phase, while in fast ion conductors, the experimental time resolution does not allow to resolve the lattice site hopping constants on the order of nanoseconds. In

[a)] These authors contributed equally.

particular, in polycrystalline fast ionic conductor materials it is expected that within a crystalline domain the quadrupolar frequency ω_Q is motionally averaged by fast hopping leading to a residual effective quadrupolar frequency. Changes in this residual value by slower inter-domain hopping being in the experimental time resolution are expected to be the main sources of measurable signal in the SAE experiment.[6,9]

To address these shortcomings, we are targeting the model system $Li_{10}GeP_2S_{12}$ (LGPS) in this work. This system is first of all technologically relevant as its fast ion transport renders it a promising energy material for battery application. Secondly, it is well suited due to the availability of detailed quadrupolar NMR data in the literature.[6,7,23–26]. First reported in 2011 with one of the highest solid state ionic conductivities[27], LGPS crystallizes in two phases: tetragonal and orthorhombic. The tetragonal phase (*t*-LGPS) shows excellent transport, with an ionic conductivity of about 12 mS/cm, arising predominantly from fast channel diffusion. By contrast, the orthorhombic LGPS (*o*-LGPS) is typically observed as a side phase and is expected to display inferior transport properties.[23,28]

In this work, we simulate an end-to-end SAE experiment, which we will refer to as a spin alignment dynamics (SAD) simulation, for the fast ion conductor LGPS. In Section II we show an ML workflow analogous to previous work[22], coupling an ML interatomic potential with a tensorial ML model to compute time dependence of quadrupolar observables. In Section III A, we show that using this workflow, we can match the motionally narrowed quadrupolar coupling constant in *t*-LGPS, which the static approach fails to do. Furthermore, we perform an SAD simulation for different LGPS phases in Section III B. We advance SAD postprocessing by incorporating the ILT methodology and discussing its applicability to simulated data. This methodology allows us to obtain the distribution of time constants from one SAD-ACF without prior assumptions of underlying ACF timescales and functional form. Moreover, we demonstrate that the ILT methodology captures both the relevant timescales of the underlying atomistic kinetics and the associated energetics by enabling the extraction of activation energies.

Finally, we extend our methodology from bulk crystals to grain boundaries and investigate ^{7}Li-ion transport across a *t*-LGPS grain boundary, which is believed to be the main source of measurable signal in the SAE experiment. Using ILT, we recover not only the bulk hopping time constants but also the timescales of intergranular population exchange. In doing so, we reach experimentally relevant length and timescales and emulate *in silico* an SAE experiment, including the full signal-processing and analysis pipeline.

II. METHODS

A. Training of Machine Learning Surrogate Models

To simulate the time evolution and time averaging of NMR observables, we utilize the methodology introduced in previous work.[22] Two independent ML models are used; the first

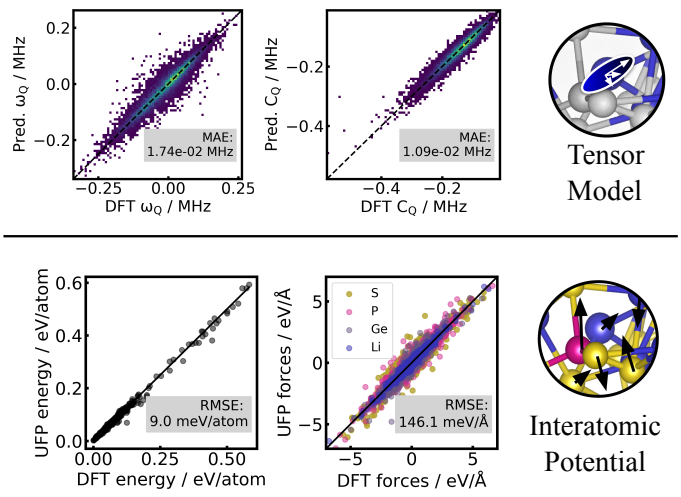

FIG. 1. ML surrogate models trained on LGPS. Top: λ-SOAP model trained on ^{7}Li EFGs with performance evaluated for the tensorial observables ω_Q (left) and C_Q (right). Colors denoting data point density from dark blue (low) to yellow (high). Bottom: UFP trained on energies and forces of all elements with performance evaluated for energies (left) and forces (right). Colors denote lithium (blue), germanium (purple), phosphorus (pink), and sulfur (yellow).

one an ML interatomic potential to simulate the dynamics of LGPS on an atomic level and a second, tensorial model to predict the EFG tensor, from which to derive the quadrupolar frequency ω_Q along the simulated trajectories. As an interatomic potential, the ultra–fast–potential (UFP)[29] is chosen, which fulfills our needs of accuracy while providing the performance of a comparable classical force field. The tensor prediction is performed with tensorial ML as introduced by the λ-SOAP descriptor,[30] which has the capability to predict the NMR observables at experimental accuracy.[16,22] Both ML models are trained on the same DFT reference dataset using an iterative training scheme. For more details, refer to the supporting information, Sec. I. The training dataset for both models consists of data from three different phases: *t*-LGPS (including P-Ge occupational disorder), *o*-LGPS, and amorphous LGPS (*am*-LGPS). Finally, we test the model performance on a withheld dataset containing all structure classes. As depicted in Fig. 1, both models reach a comparable performance to the one reported previously by Harper *et al.* for LPS[22] with slightly elevated errors, which can be explained by the increased temperature range and higher diversity of structures employed in this work. In the case of the tensorial model, the prediction of the C_Q observable reaches a higher accuracy (MAE: 11 kHz) than for ω_Q (MAE: 17 kHz), as the angular components of the EFG are more challenging to learn by the ML methodology.[16] Additionally, the ion diffusion in *t*-LGPS predicted by the UFP model is compared with *ab initio* molecular dynamics (AIMD) for validation, reaching an excellent agreement (supporting information Sec. II).

B. Molecular Dynamics Simulations and Building of Grain Boundary Structures

All molecular dynamics (MD) simulations are performed using the LAMMPS simulation software[31], using the UF3 pair style[29] with a time step of 2 fs. The structures are equilibrated using subsequent NpT and NVT ensembles within the Nosé-Hoover thermostat.[32] Production runs are then executed in an NVE ensemble.

We utilize the Aimsgb package[33], which is based on pymatgen[34] to create grain boundaries of coincident site lattice nature with a vacuum layer between two tilted grains. Due to the mixed covalent-ionic nature of LGPS, bonds of thiophosphate building blocks are cut in the procedure. The building blocks are completed and unbound sulfur atoms are removed. Then, a thin amorphous domain in the grain-grain boundary region is sampled and the grains are compressed until the amorphous domain reaches a density approaching that of the crystal. The scheme follows the approach introduced by Stegmaier *et al.*.[35]

C. Experimental Spin Alignment Echo with Inverse Laplace Transform

This work does not present any new experimental results. Yet, comparison of the simulation results with experiments from literature[6–8,23] requires a short introduction to the concepts of both experiment and simulation and their differences.

For nuclei with a non-vanishing quadrupolar moment (i.e., $S > 1/2$), the nuclear electric quadrupole moment Q couples with the local EFG tensor $\mathbf{V}$ adding the quadrupolar coupling term to the spin Hamiltonian. To first order, the interaction is proportional to the quadrupolar frequency[36,37]

$$\omega_Q = \frac{3\pi C_Q}{2I(2I-1)}\left[3\cos^2(\theta) - 1 - \eta\sin^2(\theta)\cos(2\phi)\right], \quad (1)$$

which depends on the magnitude of the EFG tensor $\mathbf{V}$ given by the quadrupolar coupling constant C_Q, on its shape defined by the asymmetry parameter η as well as on its orientation relative to the external magnetic field determined by the polar θ and azimuthal angles ϕ.[38] The SAE NMR experiment detects the spin-echo and its decay caused by fluctuations in the resonance frequency due to ion hopping between spectroscopically inequivalent sites. The decorrelation of the resonance frequency is caused either by fluctuations in the dipolar coupling or the quadrupolar frequency. While Paulus *et al.* have studied the dipolar contribution for LGPS[6,7], we restrict our study to the dominating quadrupolar contribution to SAE. The echo amplitude is a measure of the probability of finding a Li ion at time t in the spectroscopically identical position as its initial one and is proportional to the ACF of ω_Q approximated by[22]

$$\mathrm{ACF}(t) = \langle \omega_Q(t=0)\cdot\omega_Q(t)\rangle, \quad (2)$$

where the ensemble average $\langle\cdot\rangle$ is taken over all Li atoms in the sample.

In comparison to stretched exponential fitting of the ACF, ILT is superior in resolving a continuous distribution of correlation times of ionic motion.[39] A signal s_R in the time domain, here assumed one-dimensional, can be related to a joint distribution $\mathscr{G}(\tau)$ of variables τ by a Fredholm integral of the first kind

$$s_R(t) = \int_0^\infty k(t,\tau)\mathscr{G}(\tau)\,d\tau + \varepsilon(t), \quad (3)$$

where the kernel k is a known user defined function and ε models the noise contribution to the signal. In order to get the spectrum $\mathscr{G}(\tau)$ of time constants τ from a known signal s_R (i.e. an ACF), the integral in Eq. 3 must be inverted. The vectorization of the integral yields

$$\boldsymbol{s} = \boldsymbol{K}\boldsymbol{g} + \boldsymbol{e}, \quad (4)$$

where $\boldsymbol{s}$, $\boldsymbol{K}$, $\boldsymbol{g}$ and $\boldsymbol{e}$ are the vectorization of the signal, the kernel, the spectrum and the noise, respectively.

However, because the employed kernel (typically exponential or Gaussian) cannot span all possible functional spaces, and due to the presence of noise in the signal, the inversion problem becomes ill-conditioned,[40] preventing a stable solution from being obtained through direct inversion. To stabilize the inversion, the ILT inversion has been based on Tikhonov regularization using uniform penalty regularization with an additional zero-crossing of the density function penalty term[39] (see supporting information Sec. VIII). The latter being preferred to a non-negativity constraint which is not always physically justified[41]. Consequently, a regularizing penalty term is added and the vectorized solution $\hat{\boldsymbol{g}}$ of the inversion problem is given by[39]

$$\hat{\boldsymbol{g}} = \mathrm{argmin}\{\|\boldsymbol{K}\boldsymbol{g} - \boldsymbol{s}\|_2^2 + \alpha_{00}^2\|\boldsymbol{\Lambda}\boldsymbol{g}\|_2^2\}, \quad (5)$$

where Λ is the regularization matrix which contain coefficient matrices for amplitude, slope and curvature regularization while α_{00} is a global scaling factor for the regularization matrix. Eq. 5 is solved iteratively until convergence is reached.

D. Spin Alignment Dynamics with Inverse Laplace Transform

The SAE experiment and the SAD simulation differ in four major points. First, as mentioned above, the simulations presented in this work neglect the dipolar coupling contributions. Second, the propagation of the system in time is performed via MD simulations running up to 1 µs, while the SAE experiment is sensitive to ionic mobility in the range of ≈10 µs to seconds. Third, an echo can be measured only for ionic motions for which timescales are $> 1/C_Q$ (∼10 – 100 µs) as faster dynamics get averaged out. In contrast, simulations can theoretically produce the ACF on much finer time grids (down to ∼ps and even ∼fs in this work). Strictly speaking, simulations only emulate the SAE echo decay by directly computing the quadrupolar frequency ACF albeit on a different timescale while the signal inversion workflow is kept analogous. Finally, experimental samples contain on the order of

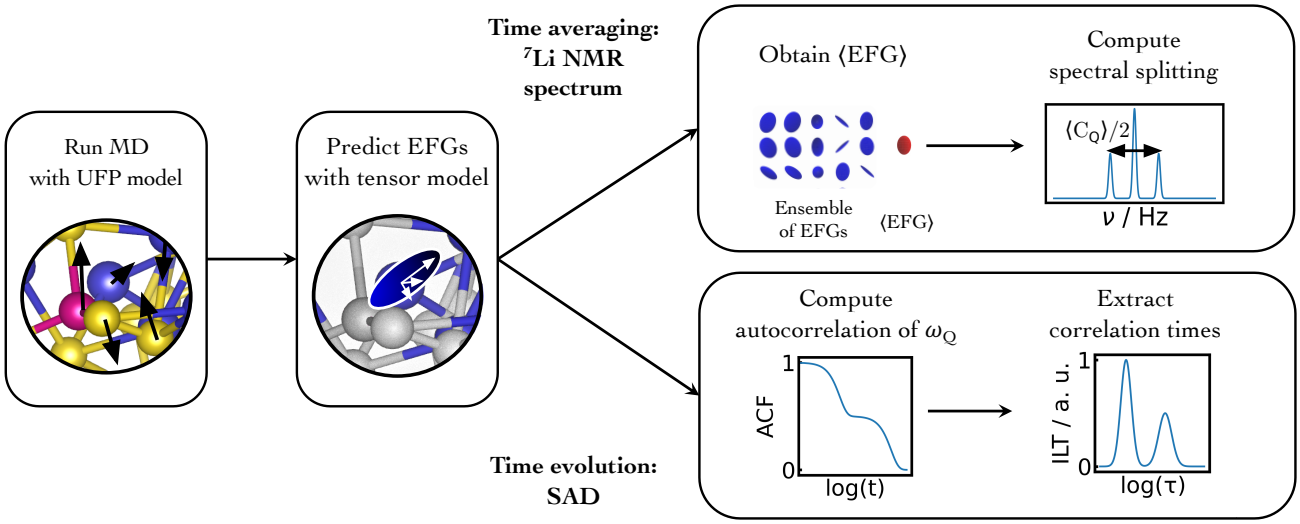

FIG. 2. Schematic workflow for the two simulated experiments in this paper: ^{7}Li NMR spectrum (time averaging of EFG tensor) and SAD (time evolution of EFG tensor). Same color code as in Fig. 1.

10^{20} atoms, while simulation cells are finite with about 10^3 atoms.

Using the tensorial ML model trained as described in Sec. II A and Fig. 2, the ^{7}Li EFG tensors are predicted along the MD trajectories by sampling the latter at equidistant time intervals Δt_{EFG} larger than the MD integration timestep (2 fs), and computing the EFG tensors at each sampled point. From the predicted tensors, the quadrupolar frequencies are then calculated according to Eq. 1, which are subsequently used to evaluate the ACF as defined in Eq. 2.

Since the simulated ensemble average in Eq. 2 can only draw from a limited number of atoms in comparison to experiment, the ACF will inevitably exhibit fluctuations. Consequently, the finite-size effects in simulations manifest as significant noise in the decaying signal, which hinders the extraction of useful information when performing the ILT. To reduce noise in the signal, the MD trajectory is randomly segmented by sampling N_s segments and computing the corresponding ACF_i, each of 80% length of the full simulation. The length of the segments is chosen in order to compromise noise reduction and signal length losses. The resulting ACF_i are then averaged

$$\overline{\mathrm{ACF}}(t) = \frac{A}{N_s}\sum_{i=1}^{N_s}\mathrm{ACF}_i(t), \tag{6}$$

and the resulting smoothed $\overline{\mathrm{ACF}}$ is normalized $\overline{\mathrm{ACF}}(t=0) = 1$ with the normalization factor A . Because the system is assumed to be in equilibrium, in accordance with the ergodic hypothesis, the absolute choice of the time origin $t = 0$ in Eq. 2 is irrelevant, and each segment constitutes a valid realization of the signal. To maximize the smoothing, the difference between each segment starting time is chosen as small as possible ($\geq$ 1 ps) given the available EFG sampling time step therefore maximizing the number of segments employed.

It must be noted that processes occurring over widely different timescales contribute unequally to the number of points in the ACF. Longer timescale decays arise from more points and thus their weight in the penalty term in Eq. 5 is disproportionately higher. To balance the fast and slow process contributions, the ILT is performed on a logarithmically sub-sampled $\overline{\mathrm{ACF}}$ (see supporting information, Sec. IX).

To evaluate the effectiveness of the smoothing of the ACF to reduce the noise level, we define a global signal–to–noise ratio (SNR)

$$\mathrm{SNR} = \frac{1}{\sigma}, \tag{7}$$

where σ is the standard deviation of the noise. This definition follows from the work of Choi *et al.* who performed ILT on synthetic exponential decays and studied the inversion effectiveness.[42] They recommend an SNR $\geq$ 40 for reliable feature detection. The standard deviation of the noise is estimated from the residuals of the ILT and due to the logarithmic sampling, a weighting by data points (signal-power-to-noise-power ratio) is not necessary.

By inverting randomly segmented, logarithmically sampled ACFs (Eq. 6), spurious features tied to individual realizations can arise. To mitigate artifacts, we construct a robust ILT spectrum by determining the median of $M = 20$ spectra $\hat{g}$ derived from M independent, randomly segmented $\overline{\mathrm{ACF}}$. By using the median, we prevent distortion of the final spectrum by spurious peak over–sharpening artifacts that manifest as unusually high intensities.

To quantify the detectability of individual peaks in the ILT spectrum, we introduce a peak-specific signal-to-noise ratio, $\mathrm{SNR_P}$, which is obtained by weighting the global ACF-SNR (Eq. 7) by the fractional area of each ILT peak $A_{\mathrm{pk}}/A_{\mathrm{tot}}$

$$\mathrm{SNR_P} = \frac{A_{\mathrm{pk}}}{A_{\mathrm{tot}}}\mathrm{SNR}. \tag{8}$$

https://doi.org/10.26434/chemrxiv-2025-ljd30 **ORCID:** https://orcid.org/0009-0007-7110-2003

Physically, A_{pk}/A_{tot} represents the portion of ACF decay attributable to that spectral component and is obtained by integrating a Gaussian fit to each peak (see supporting information, Sec. VI). The resulting SNR_P is dimensionless and indicates directly how prominently each peak's contribution stands out above the noise level.

In addition to the SNR, the time interval of EFG sampling as well as the length of the MD trajectory impact the ILT and determine the likelihood of artifacts in the ILT spectra. Our studies show that the time interval for the EFG sampling Δt_{EFG} must ensure that the ACF signal contains a sufficiently dense representation of the relevant dynamics τ, specifically $20\,\Delta t_{EFG} < \tau_{min}$ where τ_{min} is the fastest timescale the ILT can resolve without artifacts. Furthermore, the total MD trajectory t_{MD} must be long enough for the ILT to cover the full information associated with that timescale. To prevent distortions in the reconstructed spectrum, $t_{MD} > 5\tau_{max}$, where τ_{max} is the slowest timescale the ILT can resolve without artifacts. Beyond τ_{max}, the choice of exclusively exponential kernels and the assumption of a smooth distribution of τ are no longer suitable, since the sampling of the long timescale dynamics is cut off by the MD limit t_{MD}. Based on the considerations above, we define the ILT validity domain (ILTVD) within the bounds of τ_{min} and τ_{max} as the portion of the ILT spectrum where, according to the data sampling, no spectral artifacts are expected.

The parametrization of the ILT is performed using the IltPy python package[43] that facilitates the analysis of relaxation (see supporting information, Sec. VIII).

III. RESULTS

A. Simulation of ^{7}Li Quadrupolar Coupling in Single Crystal

In this section, we demonstrate the power of our dynamic computational NMR methodology by simulating the spectral features, quadrupolar coupling constant C_Q, and asymmetry η for the ^{7}Li NMR spectrum of crystalline LGPS. Considering dynamic averaging by ionic motion proves crucial in order to reproduce and understand the temperature dependent experimentally measured quadrupolar observables. We will explain the simulation of spectra and compare them to experiment for *t*-LGPS. Subsequently, we will also predict spectra for the side-phases *o*-LGPS and *am*-LGPS.

t-LGPS is a periodic crystalline material, which features occupational disorder on the P/Ge sites as well as partial occupancy of the four distinct Li sites: 16*h* and 8*f* in the highly conductive z-channels as well as 4*c* and 4*d* as connecting sites outside the channels (Fig. 3a). The partial occupancy contributes to the excellent transport properties.[27,44]

Tensor simulation on the pristine unit cell of *t*-LGPS (50 atoms) yields C_Q values of the four distinct lattice sites in the range of 100-160 kHz (Fig. 3b, middle). DFT calculations yield qualitatively the same result with identical ordering but slight shifting of peaks (supporting information, Sec. III). In contrast, Paulus *et al.* reported an experimentally determined C_Q of *t*-LGPS powder at room temperature of 23 kHz.[6]. The discrepancy originates from the high ionic conductivity of Li in *t*-LGPS, where the hopping frequencies are found to be in the GHz regime.[28,45] Hence, the Li ions are expected to sample all Li lattice sites within one period of $1/C_Q$ through fast hopping

$$\tau_{hop} \ll \frac{1}{C_Q}. \tag{9}$$

In order to account for the inter-site Li hopping, a weighted average of the EFG tensors of the four lattice sites is performed, which reduces the derived C_Q to a value of 48 kHz (Fig. 3b, bottom) The effective C_Q is still a factor of two larger than the experimental value. Averaging the EFGs of the 0 K structural model fails to consider the thermal motion of the Li ions and the lattice. Sampling along an MD trajectory takes the vibrational degrees of freedom into account as well as fast Li hopping mechanisms.

Following the workflow depicted in Fig. 2, the EFG tensors are sampled along a $t_{MD} = 40$ ns MD trajectory at 300 K, using a 3x3x3 supercell of *t*-LGPS containing 1350 atoms (with $N_{Li} = 540$ Li atoms) and a sampling interval for the $\mathbf{V}$ tensor predictions of $\Delta t_{EFG} = 1$ ps. The convergence of the computed C_Q with respect to the simulation cell size was confirmed (see supporting information, Sec. III). The distributions of the derived C_Q values for the different lattice sites are shown in Fig. 3c. For ^{7}Li, the ensemble- and time-averaged EFG tensor $\langle\mathbf{V}\rangle_{t,\mathrm{Li}}$, tensor-averaged $C_Q^{\langle\mathbf{V}\rangle_{t,\mathrm{Li}}}$, and tensor-averaged $\eta^{\langle\mathbf{V}\rangle_{t,\mathrm{Li}}}$ over N_{snap} snapshots and N_{Li} Li ions are computed by

$$\langle\mathbf{V}\rangle_{t,\mathrm{Li}} = \frac{1}{N_{snap}\cdot N_{Li}} \sum_{i=0}^{N_{snap}} \sum_{j=0}^{N_{Li}} \mathbf{V}_j(t_i), \tag{10}$$

$$C_Q^{\langle\mathbf{V}\rangle_{t,\mathrm{Li}}} = \frac{e^2Q}{h} \langle\mathbf{V}\rangle_{t,\mathrm{Li}}^{zz}, \tag{11}$$

$$\eta^{\langle\mathbf{V}\rangle_{t,\mathrm{Li}}} = \frac{\langle\mathbf{V}\rangle_{t,\mathrm{Li}}^{xx} - \langle\mathbf{V}\rangle_{t,\mathrm{Li}}^{yy}}{\langle\mathbf{V}\rangle_{t,\mathrm{Li}}^{zz}}, \tag{12}$$

where $\langle V\rangle_{t,\mathrm{Li}}^{zz}$ is the largest absolute eigenvalue of the averaged $\langle\mathbf{V}\rangle_{t,\mathrm{Li}}$. Ergodicity is assumed on this timescale and emulated through the ensemble average over the ensemble of N_{Li} Li ions (for more detail refer to supporting information, Sec. IV).

The tensor averaging yields an effective $C_Q^{\langle\mathbf{V}\rangle_{t,\mathrm{Li}}}$ of 24 kHz, which is in excellent agreement with the experimental value of 23 kHz at the same temperature. Experiments also yield an estimate for the asymmetry, which is reported as "nearly zero" for *t*-LGPS.[23] The MD-based simulations reproduce the negligible tensor-averaged asymmetry very well with $\eta^{\langle\mathbf{V}\rangle_{t,\mathrm{Li}}} = 0.05$. Using the tensor-averaged quantities $C_Q^{\langle\mathbf{V}\rangle_{t,\mathrm{Li}}}$, $\eta^{\langle\mathbf{V}\rangle_{t,\mathrm{Li}}}$ and $\omega_Q^{\langle\mathbf{V}\rangle_{t,\mathrm{Li}}}$ can be computed. The quadrupolar frequency has an angular dependence and thus is not independent of the reference frame orientation. By sampling the unit sphere of orientations uniformly, a distribution of $\omega_Q^{\langle\mathbf{V}\rangle_{t,\mathrm{Li}}}$ values is obtained and plotted in Fig. 3d with its negative counterpart

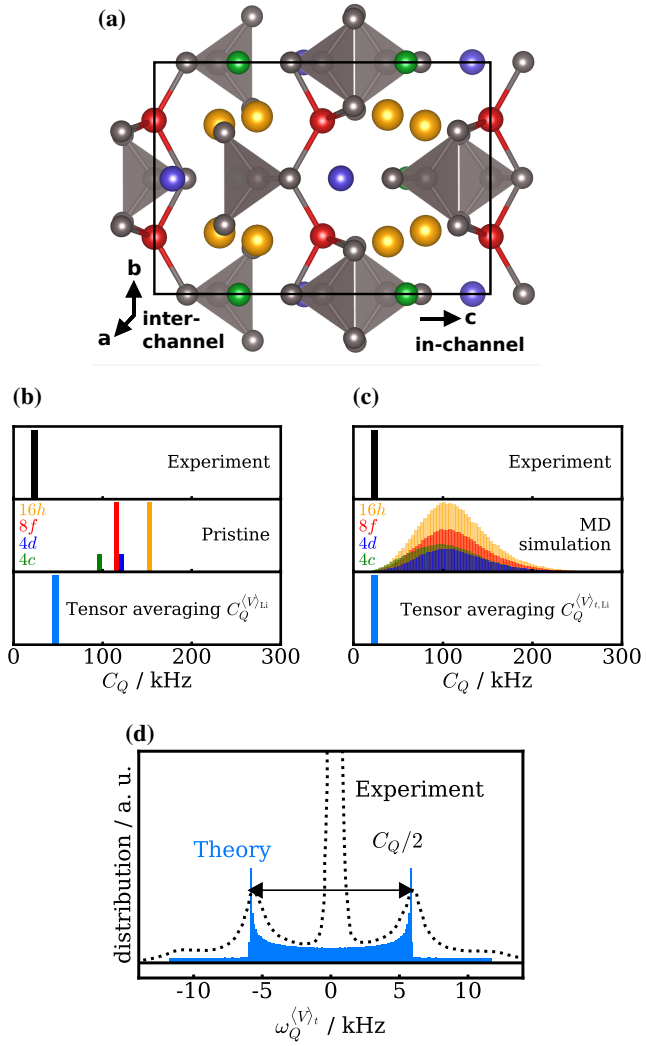

FIG. 3. **a)** Crystal structure of *t*-LGPS with the four Li lattice sites 16*h* (red), 8*f* (orange), 4*c* (green), and 4*d* (blue). **b)** Static approach: simulation of C_Q values of the respective Li lattice sites and estimate of C_Q from an averaged tensor of all sites, assuming the Li hopping is at a much higher rate than the quadrupolar coupling. **c)** Dynamic approach: as in (b) but including MD-derived distributions of C_Q within each site; the final $C_Q^{\langle\mathbf{V}\rangle_{t,\mathrm{Li}}}$ from the tensor distribution agrees with experiment. **d)** Computational and experimental[6] Pake pattern of *t*-LGPS.

($\eta^{\langle\mathbf{V}\rangle_{t,\mathrm{Li}}} \approx 0$). The powder Pake pattern and the satellite peak splitting of the experimental spectrum[6] of *t*-LGPS is reproduced correctly.

Tensor-averaged observables are also predicted for the side phases, *o*-LGPS and *am*-LGPS, with t_{MD} = 1µs and summarized in Tab. I. For *o*-LGPS, the tensor averaging yields $C_Q^{\langle\mathbf{V}\rangle_{t,\mathrm{Li}}}$ = 29 kHz (exp: 22 kHz) and $\eta^{\langle\mathbf{V}\rangle_{t,\mathrm{Li}}}$ = 0.16 (exp: "nearly zero"). The agreement with experiment is less accurate than for *t*-LGPS, which might be attributed to two reasons. First, as the Li diffusion in *o*-LGPS is much slower than in *t*-LGPS, the diffusion mechanism might be sampled insufficiently within a 1 µs MD trajectory. Secondly, the unit cell adopted from Materzanini *et al.* is obtained purely from theory by geometry optimisation of the related *o*-LGPO structure and might thus deviate from the true experimental one.[28]

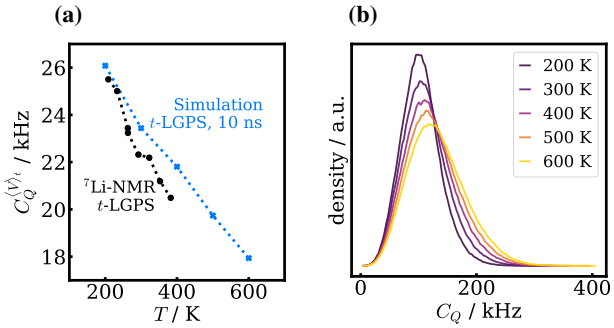

FIG. 4. **a)** Temperature dependence of C_Q in *t*-LGPS, theory and experiment[7]. **b)** C_Q distributions from MD simulations of *t*-LGPS at different temperatures.

TABLE I. Observables $C_Q^{\langle\mathbf{V}\rangle_{t,\mathrm{Li}}}$ and $\eta^{\langle\mathbf{V}\rangle_{t,\mathrm{Li}}}$ at 300 K as derived by simulations performed on supercells of the ideal crystals and on an amorphous supercell model, respectively, as well as experimental values from literature.

System	$C_Q^{\langle\mathbf{V}\rangle_{t,\mathrm{Li}}}$ / kHz	$\eta^{\langle\mathbf{V}\rangle_{t,\mathrm{Li}}}$	t_{MD} / ns	N_{Li}
t-LGPS	24	0.05	40	540
o-LGPS	29	0.16	1000	480
am-LGPS	2	0.68	1000	640
exp. *t*-LGPS[6]	23	0		
exp. *o*-LGPS[7]	22	0		

For the amorphous case, a much smaller $C_Q^{\langle\mathbf{V}\rangle_{t,\mathrm{Li}}}$ of 2 kHz is predicted by simulation. Since the amorphous structure lacks symmetry and periodic order, the Li experiences more diverse environments along its trajectory resulting in a more complete isotropic averaging of the tensor, which is also in line with experimental findings.[23] $\eta^{\langle\mathbf{V}\rangle_{t,\mathrm{Li}}}$ is predicted to be 0.68, however, for tensors of very small magnitude, the notion of asymmetry ceases to be well defined.

The phenomenon of spectral averaging at finite temperature is widely known as motional narrowing and is temperature dependent. Motional narrowing can be explained by the EFG property of tracelessness. By averaging more and in particular more diverse EFG shapes and orientations, a time averaged EFG tensor naturally becomes more spherical, yielding eigenvalues of smaller magnitude and a smaller asymmetry. Motional narrowing for different solids has been reported repeatedly from experiment.[9,46,47] It has been also studied in computational approaches, which only included the materials vibration but did not take into account the potential hopping.[19,21,48] We probe the temperature dependence of the simulated $C_Q^{\langle\mathbf{V}\rangle_{t,\mathrm{Li}}}$ estimates for *t*-LGPS in Fig. 4a and find a trend of linearly reducing $C_Q^{\langle\mathbf{V}\rangle_{t,\mathrm{Li}}}$ in the temperature range of 200-600 K. Comparison with experimental values[6,23] show a similar trend with

slightly (by 1-2 kHz) lower experimental C_Q values, but overall a good correspondence with our simulations. It should be emphasized that the experimental sample is a powder with potential contributions from side phases, while an idealised single crystal model system is studied here.

From a physical point of view, the further linear reduction of the C_Q observable with elevated temperature cannot be attributed to the Li sampling more diverse lattices sites with faster hopping, since the hopping constants at 300 K are already faster than $1/C_Q$.[7,24] The effect is more likely related to a more thorough exploration of the potential energy surface within the lattice sites or a more pronounced influence of site disorder. Fig. 4b shows the distribution of C_Q including all lattice sites within a temperature range of 200-600 K. A slight broadening effect is observed at elevated temperatures.

B. Spin Alignment Dynamics Simulation

Having demonstrated the accurate prediction of motionally narrowed quadrupolar observables, their time evolution is now examined. An SAD simulation is performed in which we emulate the experimental echo decay by computing the ^{7}Li quadrupolar frequency ACF as explained in Sec. II D. In order to accurately reproduce an experimental SAE decay measurement, the quadrupolar frequency of each Li ion at each time step should ideally be replaced by the value obtained from the time-averaged EFG tensor over a duration of $1/C_Q$ (approximately 50 µs). However, this timescale exceeds the accessible simulation timescales (∼1 µs), and thus the ACF is computed directly from the instantaneous quadrupolar frequencies at each time step. This approximation might affect the magnitude of decay, but does not affect the characteristic timescale over which the quadrupolar frequency decorrelates. Consequently, the simulated SAD decay not only provides qualitative statements on which dynamic processes are potentially SAE active, but also impact longitudinal relaxation processes.

1. SAD of Single Crystal LGPS

Starting with the bulk phases of *t*-LGPS, *o*-LGPS, and *am*-LGPS, the computed smoothed $\overline{\mathrm{ACF}}$ obtained from MD simulations at 300 K are shown in Fig. 5a. The different simulation durations reflect the distinct timescales required for the Li quadrupolar decorrelation in each system. All smoothed ACFs display the same qualitative behavior. They all exhibit a large rapid initial decay within the first picoseconds followed by a smaller and more gradual decay, which converges to a baseline value.

The initial ultrafast decay is attributed primarily to lattice vibrations that perturb the local EFG and occurs on timescales shorter than the EFG sampling Δt_{EFG} of picoseconds. Hence, it is depicted as an interpolated, dashed line in Fig. 5a. For *t*-LGPS, it is shown that the MD-ML approach also allows to resolve the vibrational regime by predicting the EFGs tensors on a fine time grid ($\Delta t_{\mathrm{EFG}} = 2$ fs) up to 10 ps, from which the corresponding ACF is computed (translucent blue in Fig. 5a).

TABLE II. Computed ACF asymptotic baselines values for all LGPS bulk phases reflecting the different degree of symmetry of the system.

System	*t*-LGPS	*o*-LGPS	*am*-LGPS
$\langle\omega_{\mathbf{Q}}\rangle^2/\langle\omega_{\mathbf{Q}}^2\rangle$	10.2×10^{-3}	6.9×10^{-3}	1.4×10^{-3}

In contrast, probing the ACF decay arising from ion hopping requires longer simulations with a coarser EFG sampling time step Δt_{EFG}. Simulations are therefore extended until full decorrelation of the ACF is reached with a maximum limit of 1 µs. Most of the correlation in ω_Q at the Li sites is lost due to vibrations (initial, large decay) before ion diffusion to neighboring sites can occur.

To understand the origin of the computed ACF magnitude drops, we derive a simplified double component model in the supporting information (Sec. X), where we assume that the quadrupolar frequency consists of a phonon ω_{ph} and a ^{7}Li hopping contribution ω_{hop} taken as independent random variables, yielding $\omega_Q = \omega_{\mathrm{ph}} + \omega_{\mathrm{hop}}$. It follows that the correlation losses in the ACF due to phonon vibrations Δ_{ph} and ion-hopping Δ_{hop} are given by

$$\Delta_i = A\,\mathrm{Var}(\omega_i), \quad i = \{\mathrm{ph},\ \mathrm{hop}\}, \tag{13}$$

where A is the ACF normalization constant and $\mathrm{Var}(\cdot)$ denotes the variance. Since phonon-induced fluctuations of ω_Q at a given site are much larger than changes in residual site-specific quadrupolar frequencies, $\Delta_{\mathrm{ph}} \gg \Delta_{\mathrm{hop}}$, the fast and more pronounced correlation loss is explained by lattice vibrations and the slower correlation loss of smaller magnitude by ion hopping. Eventually, the ACFs converge toward a baseline, which encodes information about the overall distribution of ω_Q. Under the assumption of fully equilibrated Li within the simulated cell, the asymptotical baseline value that the ACF approaches can be estimated (see supporting information, Sec. X) and is given by

$$\mathrm{ACF}(t\to\infty) = \frac{\langle\omega_Q\rangle^2}{\langle\omega_Q^2\rangle}. \tag{14}$$

The baselines for the three different phases are computed (see Tab. II) and shown in Fig. 5a by horizontal dotted lines. For *am*-LGPS, the baseline value is an order of magnitude lower than those of the crystalline phases. In a perfect amorphous phase, one expects the ACF to decay to zero, since the structural disorder causes the EFG tensor to sample all orientations, yielding a residual $\langle\omega_Q\rangle$ of zero.

The simulated residual most likely arises from the finite size of the simulation cell (640 Li atoms). In contrast, the finite baselines of the crystalline phases reflect Li occupying specific lattice sites in a symmetric, periodic lattice, resulting in the EFG tensor sampling a limited set of orientations and hence resulting in a larger finite residual $\langle\omega_Q\rangle$.

For *t*-LGPS, a 40 ns trajectory is sufficient for Li to decorrelate, owing to the rapid Li dynamics in this material, as evidenced by the ACF reaching the baseline value predicted by

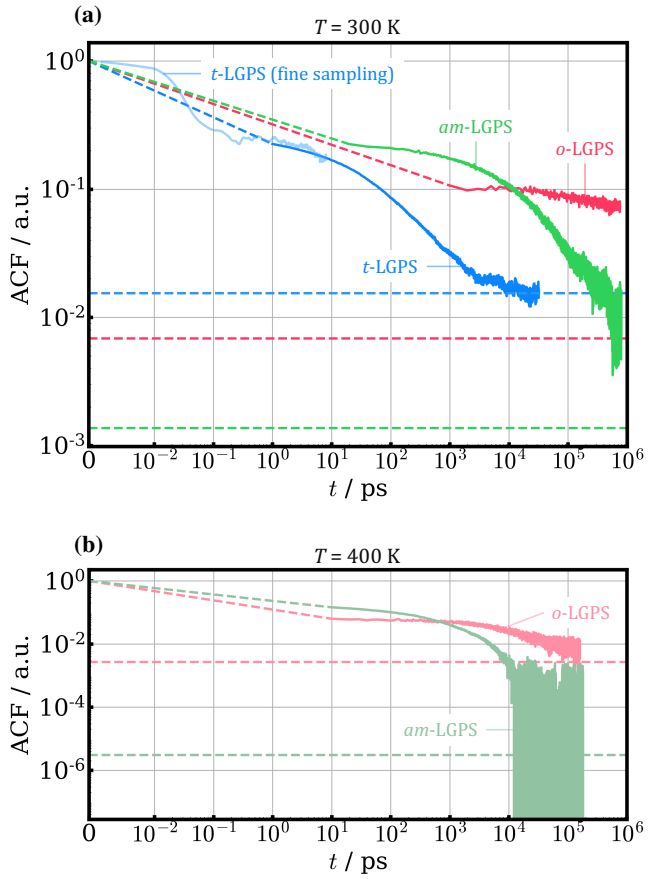

FIG. 5. **a)** ACFs of the quadrupolar frequency for bulk *t*-LGPS, *o*-LGPS, and *am*-LGPS at 300 K. The different simulation durations correspond to the varying times Li ions require to equilibrate in each phase. Horizontal dashed lines indicate the baseline values the ACF would approach under stationary conditions after full decorrelation. The decay within the first simulation time step is linearly interpolated and shown as a dashed line. For *t*-LGPS, the initial fast phonon-induced decay is additionally resolved over the first 10 ps (shown in translucent blue). **b)** ACFs for *o*-LGPS and *am*-LGPS at 400 K showing the decay to the baseline within simulation time due to faster Li hopping dynamics at higher temperatures.

Eq. 14. In *o*-LGPS and *am*-LGPS, Li dynamics are slower, and after 1 µs, a portion of the signal remains to decay in both systems. To demonstrate that this signal eventually decays, Fig. 5b shows the smoothed ACF for *o*-LGPS and *am*-LGPS at 400 K. At higher temperature, the kinetics are accelerated and the Li ions decorrelate more rapidly resulting in the ACF reaching its respective baseline value within 1 µs.

The noise level in the ACFs reflects not only the number of ^{7}Li ions, which is comparable among the different phases (see Tab. I), but more directly the number of segments N_s (see Tab. III and Eq. 6) used to construct the smoothed $\overline{\text{ACF}}$ as explained in the Sec. II D. In Fig. 5, each ACF tail shows noise that is magnified in the log–log plot as the ACF decays toward lower orders of magnitude. This suggests that further

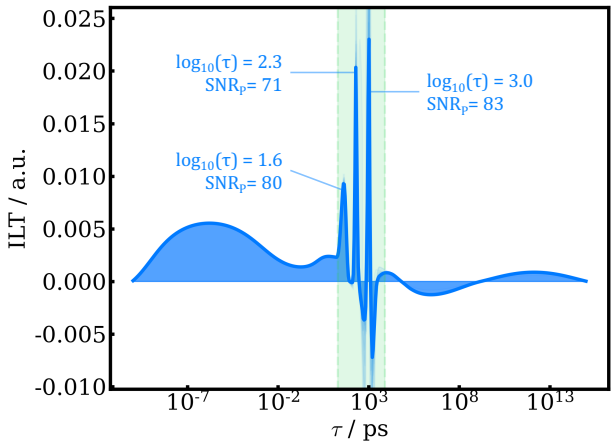

FIG. 6. ILT spectrum of bulk *t*-LGPS at 300 K. The median-averaged spectrum from $M = 20$ independent $\overline{\text{ACF}}$ realizations is plotted as a thick blue line, with individual realizations shown in translucent blue. The ILTVD is indicated in green. The SNR was estimated to be 1594.

signal drops become increasingly difficult to simulate given our data sampling, since as the ACF decays, the magnitude of these decays may fall below the noise level.

2. *ILT of Simulated SAD-ACF*

To obtain the underlying decay components, the computed ACFs from the previous section are inverted using the ILT method. For the trajectory of each phase, the corresponding ILTVD (see Sec. II C) is estimated and reported in Tab. III. Computational limitations restrict the number of atoms in the model system, the length of the trajectory, and the number of EFG-prediction steps along the trajectory, which results in an SNR that is much lower for simulated data in comparison to experimental data, making the inversion of the simulated ACF challenging (c.f. Sec. II D).

TABLE III. Simulation parameters (Δt_{EFG}: time interval of EFG sampling, t_{MD}: length of MD run and N_s: number of segment used for the smoothing of the ACF) and corresponding ILTVD of the bulk LGPS systems (300 K). The ILTVD bounds τ_{min} and τ_{max} are reported as decimal logarithms of time in picoseconds.

System	Δt_{EFG}	t_{MD}	N_s	$\log_{10}(\tau_{\text{min}}/\text{ps})$	$\log_{10}(\tau_{\text{max}}/\text{ps})$
t-LGPS	1 ps	40 ns	8000	1.3	3.9
o-LGPS	50 ps	1 µs	9500	3.0	5.3
am-LGPS	20 ps	1 µs	3800	2.6	5.3

The ILT spectrum of *t*-LGPS with the corresponding ILTVD is shown in Fig. 6. Left of the ILTVD, the spectrum exhibits a broad feature at sub-ps timescales, which originates from the extremely rapid initial decay of the ACF driven by on-site phonon vibrations (Fig. 5), which are not resolved by the coarse EFG sampling. Since the decay occurs on a

timescale orders of magnitude shorter than the sampling interval Δt_{EFG}, its signal falls outside the ILTVD, resulting in an over-broadening of the reconstructed spectrum depicting the uncertainty related to assessment of the ultrafast timescales.

Within the ILTVD, three peaks are observed at $\log(\tau) = 1.6$ ($\approx$ 40 ps), at $\log(\tau) = 2.3$ ($\approx$ 200 ps), and at $\log(\tau) = 3.0$ ($\approx$ 1 ns) with computed SNR_P values of 80, 71, and 83, respectively. The detectability of these peaks and their computed SNR_P is in line with the threshold established by Choi *et al.*[42] Within the ILTVD, individual ILT realizations exhibit fluctuations reflecting the specific noise in each ACF segmentation. By contrast, the median-averaged spectrum $\overline{ACF}$ (see Sec. II D, Eq. 6) is more robust and less sensitive to noise. The fluctuations are expected, as the regularization parameter is chosen just above the noise-fitting threshold to maximize feature resolution. Indeed, Tikhonov (L_2-norm) regularization, while enforcing smoothness by penalizing squared amplitudes, can oversmooth closely spaced components and can cause peak merging[49]. Further reduction of regularization fails to resolve additional peaks and instead introduces artifacts. Within the ILTVD, small negative features are also observed which are suspected to originate from minor oscillatory components in the ACF. Therefore, our approach regularizes only up to the point before spurious features emerge, demonstrating that the resolved peaks are separated to the fullest extent permitted by our data quality. Finally, on the right of the ILTVD, corresponding to timescales beyond τ_{max}, the median-averaged spectrum shows very broad oscillation features likely arising as boundary effects due to the finite time simulation length t_{MD}. Any component in this region represents an unwarranted extrapolation by the ILT into timescales unsupported by the original data.

We then compare the ILT peaks in *t*-LGPS with an MD-derived study (independent of NMR observables) where conditional probability of site occupancies are computed as a function of time (see supporting information, Sec. VII). Time constants for the processes are obtained via exponential fitting. Adding Gaussian broadening, a spectrum of time constants is obtained, which contains five clusters with peaks at $\log(\tau)$ = 1.9 (in-channel diffusion), 2.4, 2.8, 3.2 and 3.7 (all inter-channel diffusion). The ILT peaks at $\log(\tau)$ = 1.6, 2.3 and 3.0 are in line with the MD-derived time constants given the peak resolution allowed by the signal inversion algorithm.

Regarding the other bulk phases, Fig. 7 compares the median-averaged ILT spectra of *t*-, *o*-, and *am*-LGPS at 300 K within their respective ILTVDs listed in Tab. III. Since slower diffusion in the amorphous and orthorhombic phases is expected[28,50], the MD simulations are extended to 1 µs and the ILTVDs are adjusted accordingly.

o-LGPS exhibits a single peak at $\log(\tau) = 4.6$ ($\approx$ 40 ns), reflecting its crystalline nature and confirming that ^{7}Li diffusion is significantly slower than in *t*-LGPS. In the case of *am*-LGPS, a broad feature centered at $\log(\tau) = 3.6$ ($\approx$ 5 ns) and a peak at $\log(\tau) = 4.6$ ($\approx$ 40 ns) are observed within the ILTVD, with SNR_P values of 120 and 114, respectively. These results indicate that ^{7}Li dynamics in *am*-LGPS can be up to two orders of magnitude slower than in *t*-LGPS, and

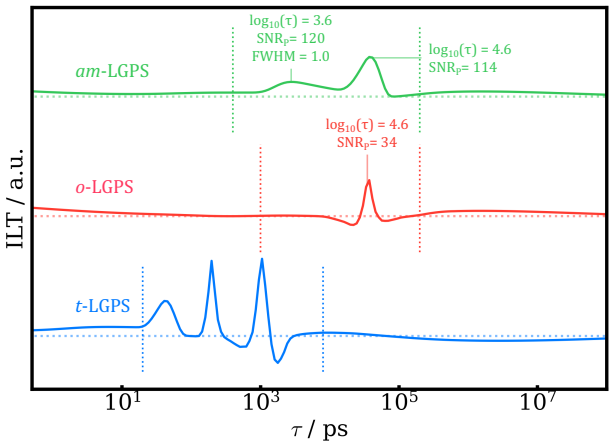

FIG. 7. Median-averaged ILT spectra of bulk LGPS phases (*t*-LGPS, *o*-LGPS, and *am*-LGPS) at 300 K. Each spectrum is obtained from $M = 20$ independent ACF realizations. Vertical dashed lines denote the ILTVD boundaries for each phase. The corresponding SNR levels are 1438, 1242, and 1594 for *am*-LGPS, *o*-LGPS, and *t*-LGPS, respectively.

the broad distribution is consistent with the amorphous structure, which gives rise to a range of local environments. The peak at $\log(\tau) = 4.6$ is sharper than expected for a disordered phase and may result from an incomplete representation of the amorphous structure, as the periodic boundary conditions constrain the system and limit the sampling of the underlying Gaussian distribution of energy barriers. As the ACFs of both *o*-LGPS and *am*-LGPS do not reach their predicted baseline values within the 1 µs simulation time, an additional ILT was performed on the 400 K simulations shown in Fig. 5b (see supporting information, Sec. XI). In both cases, the peaks consistently shift toward shorter correlation times by approximately one order of magnitude, confirming that the 300 K ILT spectra are not affected by undersampling artifacts.

3. *Temperature Dependence of the ILT Spectrum*

Further insight into Li transport properties can be gained by computing the corresponding ACFs at different temperatures and extracting energy barriers from the ILT spectral peak positions using the Arrhenius relation. In this section, the capability of our computational methodology to carry out an Arrhenius analysis is demonstrated for the *t*-LGPS bulk phase. Four MD simulations are performed at 300, 325, 350, and 400 K. The corresponding ILT spectra (Fig. 8a) show, as expected, that increasing the temperature accelerates ^{7}Li hopping dynamics, manifested by a systematic shift of all peaks to shorter correlation times. For each temperature, peak positions are determined via Gaussian decomposition (see supporting information, Sec. VI) of the spectrum and peaks that remain within the ILTVD across all temperatures are fitted with a linear model of $\log(1/\tau)$ versus $1/T$. The resulting Arrhenius plot (Fig. 8b) yields activation energies of 0.19 and

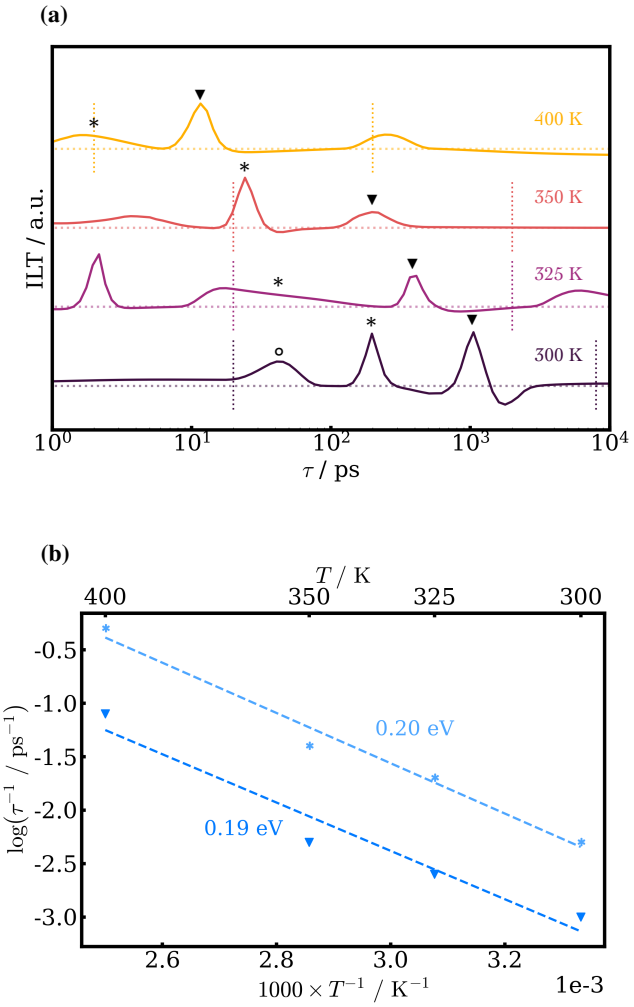

FIG. 8. **a)** ILT spectra of *t*-LGPS at 300, 325, 350, and 400 K. Peaks within the ILTVD (indicated as vertical dashed lines) across all temperatures are labeled. At 325 K, the broad feature at log(τ)=1.5 comprises two overlapping peaks (the asterisk labels the right peak), which were resolved by Gaussian decomposition. **b)** Arrhenius plot of the peak correlation times; linear fits yield effective activation energies.

0.20 eV. The values agree excellently with those from tracer diffusion based Arrhenius analysis, solely based on MD: 0.21, 0.22, and 0.18 eV along the *a*-, *b*-, and *c*-axes, respectively (3D MSD: 0.19 eV; see supporting information, Sec. II). The agreement suggests that our earlier assignment of peaks to diffusion along the crystallographic axes is consistent with identifying the asterisk- and triangle-labeled peaks in Fig. 8a as inter-channel diffusion. The peak associated with in-channel diffusion (log(τ)=1.6 at 300 K; dot-labeled) shifts outside the ILTVD at higher temperatures, making its tracking difficult. Overall, the analysis confirms that the ILT approach probes not only the relevant timescales but also the activation energetics of Li-ion hopping correctly. Our findings are consistent with previous computational estimates of activation barriers, which are reported in a range of 0.18–0.23 eV.[28,51,52]

4. *SAD of Grain Boundaries*

In LGPS, the decays observed in SAE experiments are not expected to reflect single crystal, bulk ion hopping. As demonstrated in previous sections, the relevant hopping events occur on sub–microsecond timescales, i.e. faster than the experimentally accessible time resolution.[6] The measured signal at timescales up to 10 s therefore has a poly-crystalline origin, most likely associated with grain boundaries that separate crystallites of differing orientation. The underlying mechanism follows from the tensorial nature of the EFG, which transforms as a rank-2 tensor under rotation. Two adjacent crystallites, *A* and *B*, can exhibit different residual quadrupolar frequencies, $\omega_{Q,A}^{\langle \mathbf{V} \rangle_{t,\mathrm{Li}}}$ and $\omega_{Q,B}^{\langle \mathbf{V} \rangle_{t,\mathrm{Li}}}$, not because their crystal structures differ, but because their orientations with respect to the magnetic field do. The difference in the residual quadrupolar frequencies between crystallites then gives rise to the echo decay. Accordingly, an echo decay can originate not only from site-to-site Li exchange within a crystallite, but also from inter-domain exchange between differently oriented grains, where orientation-induced differences in $\omega_Q^{\langle \mathbf{V} \rangle_{t,\mathrm{Li}}}$ drive the decay. In order to observe inter-domain exchange in the ACF, the correlation function must retain a non-zero value within the bulk phases — a feature reflected in the ACF baseline value discussed in Sec. III B 1.

While the decay time constant is invariant under rotations within an external reference frame, reorientation of the entire set of EFG tensors can modulate the echo decay amplitude. For certain relative orientations, the quadrupolar frequency distributions of two grains fully overlap and no echo decay is observed. For others, the residual quadrupolar frequencies are maximally separated, yielding the largest decay amplitude. In a polycrystalline sample, all grain orientations are sampled, and the measured echo decay is the result of a powder average.

To probe the effect of a grain boundary on the ACF, MD simulations of a Σ8[100]/(0-2-3) coincidence site lattice grain boundary of *t*-LGPS are performed at 300, 350, and 400 K. We specifically choose this grain boundary, as it has an angle close to 90 degrees between the two grains and thus will maximize the signal intensity. The ω_Q distribution (shown in Fig. 9a) is derived by rotation R_{max} of the reference frame for the complete set of EFGs **V** to maximize the difference of the distributions of grain *A* and *B* within the limits of the coincidence site lattice approximation (see supporting information, Sec. V). The distributions have a significant overlap, but possess a detectable difference in their expected linearly averaged values ($\langle \omega_Q \rangle_A$ = 2.5 kHz, $\langle \omega_Q \rangle_B$ = -3.0 kHz) as shown in Fig. 9a. While the SAD simulations target $\langle \omega_Q \rangle$ (Eq. 14), the SAE experiment is sensitive to the difference in motionally averaged, effective $\omega_Q^{\langle \mathbf{V} \rangle_{t,\mathrm{Li}}}$ defined analogously to $C_Q^{\langle \mathbf{V} \rangle_{t,\mathrm{Li}}}$ in Eq. 11. The values of $\omega_Q^{\langle \mathbf{V} \rangle_{t,\mathrm{Li}}}$ for the grain boundary model are

https://doi.org/10.26434/chemrxiv-2025-ljd30 **ORCID:** https://orcid.org/0009-0007-7110-2003

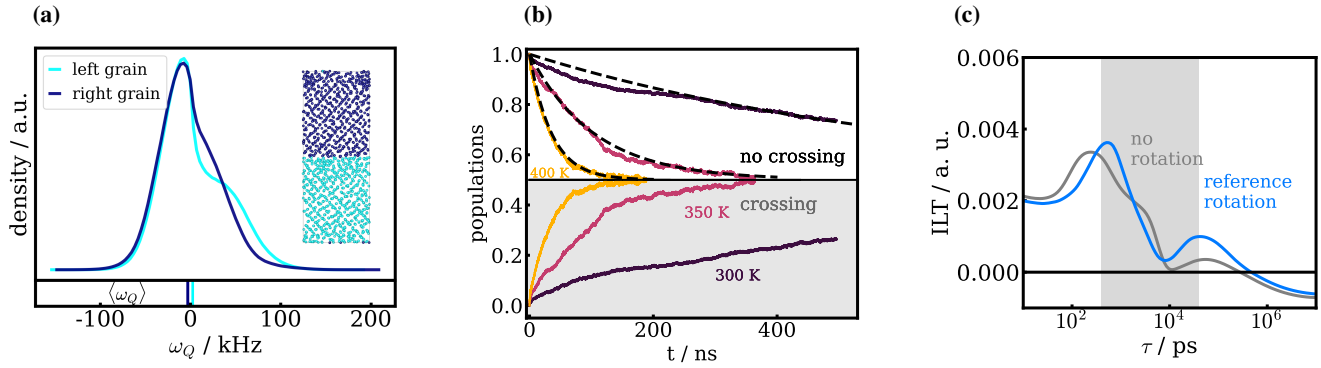

FIG. 9. **a)** Distribution of ω_Q for Li in the left and right grains of the Σ8[100]/(0-2-3) tilt grain boundary. **b)** MD analysis of population equilibration of Li at different temperatures; fitted time constants: 596 ns (300 K), 97 ns (350 K), 33 ns (400 K). **c)** ILT spectrum at 400 K, with and without rotation of the reference frame.

given by $\omega_{Q,A}^{\langle\mathbf{V}\rangle_{t,\mathrm{Li}}} = -7.8$ kHz and $\omega_{Q,B}^{\langle\mathbf{V}\rangle_{t,\mathrm{Li}}} = 3.6$ kHz.

In Fig. 9b, the conditional probabilities of Li ions to be found in their initial grain (no crossing) or in the second grain (crossing) as obtained from the MD are shown. The exponential behavior can be fitted for the three different temperatures to obtain the decay time constant of the process. The time constant at 400 K is found to be 33 ns. Because the correlation times at 350 K (97 ns) and 300 K (596 ns) exceed the ILTVD attainable within the computational limits of the MD simulations, the computational SAD framework is instead applied to the 400 K MD trajectory to probe the dynamics. The obtained ILT is shown in Fig. 9c. Two broad peaks in the ILTVD at $\log(\tau) = 2.6$ (400 ps) and $\log(\tau) = 4.6$ (40 ns) are detected. The peak at faster timescales ($\log(\tau) = 2.6$) can be attributed to bulk processes. Please note that this peak is shifted relative to the 400 K ILT of *t*-LGPS shown in Fig. 8. This shift indicates that the introduction of a grain boundary leads to a slowdown of the bulk transport. The peak at slower timescales ($\log(\tau) = 4.6$) has a corresponding decay time of 40 ns and thus is in very good agreement to the MD predicted time constant of 33 ns for the grain boundary transfer. The ILT of the grain boundary without the reference frame rotation to maximize the ω_Q distribution difference is depicted in gray, showing that the same time constant is observed, but with a much smaller signal intensity, since the ω_Q distributions are almost identical.

The grain boundary transfer we detect here is expected to play a major role in the recorded experimental data. Our predicted timescales are still significantly below the values reported in experiment, where values in the range of 100 µs to 10 ms are reported.[6] However the grain size studied here (4 nm) is orders of magnitude smaller than in the experiment, where grain sizes are estimated to be significantly larger for samples to qualify as crystalline,[50] which leads to slower expected correlation times.

IV. CONCLUSION

In this work, we have simulated the dynamic quadrupolar ^{7}Li NMR response in the fast ion conductor LGPS using an MD+ML-accelerated method. The approach enabled probing the time evolution of the EFG tensor rather than relying on a static picture of the system. In a first step, the quadrupolar coupling constant C_Q that can be measured via the ^{7}Li NMR spectrum was simulated. It was shown that by explicitly including the vibrational and hopping dynamics on a timescale faster than the quadrupolar frequency itself, the accuracy of predicted C_Q could be significantly improved in comparison to experimental data. Indeed, by explicit time-averaging of the EFG tensor, we were able to reproduce the motional narrowing and the experimental C_Q temperature dependence. In this regard, the ML-acceleration enabled simulation of bigger systems and longer timescales which are necessary to converge the underlying ensemble, yet not accessible via DFT. We suggest that motional narrowing can also play a role in other materials with pronounced vibrations and fast ion conduction, where experimental and computational estimates of quadrupolar coupling have been found to significantly disagree.[9,13]

In a second step, we performed an SAD simulation, emulating an SAE experiment which is routinely used by experimentalists to probe dynamics in ionic conductors, like hopping or inter-domain exchange. A computational SAD workflow using LPS as a bulk model system, which allowed the extraction of effective correlation time constants from an exponential fitting was already demonstrated in previous work.[22] However, in this work, we applied the ILT methodology to an SAD simulation for the first time, enabling the extraction of multiple correlation time constants. By comparing ILT-predicted signal positions and activation barriers with our MD reference, the methodology was proven be robust. Furthermore, the key factors required to obtain a reliable ILT spectrum were outlined: First of all, the SNR was maximised by a segmentation approach and also a peak specific metric was devised (i.e. $\mathrm{SNR_P}$) to understand single peak resolvability. Secondly, the formulation of the ILTVD provided a metric to identify

the spectral domain region which is free of artifacts. These considerations were crucial as computational approaches, in contrast to experiments, allow for a higher number of sample points, but are restricted in the timescale and ensemble sizes which leads to higher noise levels.

Using the ILT methodology, we investigated the dynamics in the *t*-, *o*-, and *am*-LGPS bulk phases, confirming the different timescales of EFG decorrelation. As experimental time resolution only allows to resolve timescales starting from 10 µs, the bulk signals we reported are not resolvable in measurements. The origin of the SAE signal loss is believed to originate from Li crossing different crystallites. Consequently, a more complex system containing a grain boundary of tilted *t*-LGPS crystallites was studied and the characteristic time constant of inter-domain exchange successfully captured for the first time using an *in silico* approach. We observed that the signal intensity provided by the inter-grain exchange process were small in comparison to the signal loss at faster timescales due to vibrations and bulk hopping. The grain boundary model stresses even more the importance of ML models as there is the need to sample the ensemble distributions exhaustively, which is only possible with a large sample size.

Our simulations captured time and length scales that are closer to experimental conditions than any prior theoretical approach, though they remained one to two orders of magnitude away from the true experimental scales. Future work will address this gap using further coarse graining. A suitable approach will be modeling Li diffusion by means of the kinetic Monte Carlo method, which will greatly benefit from this work by incorporating EFG tensor distributions of individual lattice sites as input parameters. Finally, we want to emphasize the importance of reproducible computational workflows as simulations grow in scope and complexity. Reducing user-adjusted parameters is key, as signal inversion remains only partially automated. Future work will link regularization strength to SNR_P and use synthetic data to probe inversion behavior. Additionally, data-driven denoising (e.g., neural networks) can be used as a systematic approach to suppress nonphysical spectral features.

AUTHOR CONTRIBUTIONS

Tabea Huss: data curation, formal analysis, investigation, methodology, visualization, project administration, writing – original draft, writing – review and editing;
Federico Civaia: data curation, formal analysis, investigation, methodology, visualization, project administration, writing – original draft, writing – review and editing;
Simone S. Köcher: supervision, writing - review and editing
Karsten Reuter: writing - review and editing, funding acquisition
Josef Granwehr: supervision, writing - review and editing
Christoph Scheurer: supervision, writing - review and editing, funding acquisition

CONFLICTS OF INTEREST

There are no conflicts of interest to declare.

DATA AVAILABILITY

The data will be published open-access on the EDMOND MPG data service[53] after acceptance.

ACKNOWLEDGEMENTS

All computational resources were provided by the Max Planck Computing and Data Facility (MPCDF). The authors acknowledge funding by the Deutsche Forschungsgemeinschaft (DFG, German Research Foundation) within the cluster of excellence EXC 2089: e-conversion. We thank Davis Thomas Daniel for providing the IltPy package and for valuable discussions.

[1] H. W. Spiess, J. Chem. Phys. **72**, 6755 (1980).
[2] R. Böhmer, K. Jeffrey, and M. Vogel, Prog. Nucl. Magn. Reson. Spectrosc. **2**, 87 (2007).
[3] M. Wilkening, A. Kuhn, and P. Heitjans, Phys. Rev. B **78**, 054303 (2008).
[4] B. Gadermaier, K. Hogrefe, P. Heitjans, and H. M. R. Wilkening, Eur. J. Inorg. Chem. **2021**, 1028 (2021).
[5] J. Langer and M. Wilkening, Solid State Ionics **293**, 85 (2016).
[6] M. Paulus, M. Graf, P. Harks, A. Paulus, P. Schleker, P. Notten, R.-A. Eichel, and J. Granwehr, J. Magn. Reson. **294**, 133 (2018).
[7] M. C. Paulus, *NMR-investigations on the lithium solid state electrolyte $Li_{10}GeP_2S_{12}$ (LGPS)*, Ph.D. thesis, RWTH Aachen University (2020).
[8] M. C. Paulus, A. Paulus, R.-A. Eichel, and J. Granwehr, Z. Phys. Chem. **236**, 899 (2021).
[9] M. F. Graf, H. Tempel, S. S. Köcher, R. Schierholz, C. Scheurer, H. Kungl, R.-A. Eichel, and J. Granwehr, RSC Adv. **7**, 25276 (2017).
[10] A. Kuhn, V. Epp, G. Schmidt, S. Narayanan, V. Thangadurai, and M. Wilkening, J. Phys.: Condens. Matter **24**, 035901 (2011).
[11] B. Koch and M. Vogel, Solid State Nucl. Magn. Reson. **34**, 37 (2008).
[12] M. Wilkening and P. Heitjans, ChemPhysChem **13**, 53 (2011).
[13] J. Valenzuela Reina, F. Civaia, A. F. Harper, C. Scheurer, and S. S. Köcher, Faraday Discuss. **255**, 266 (2025).
[14] J. V. Reina, V. M. Barysch, C. Szczuka, S. S. Köcher, J. Granwehr, and C. Scheurer, Energy Adv. **4**, 1013 (2025).
[15] S. S. Köcher, *Simulation of static and dynamic magnetic resonance parameters for solid mixed conductors*, Ph.D. thesis, RWTH Aachen University (2019).
[16] A. F. Harper, S. S. Köcher, K. Reuter, and C. Scheurer, J. Mater. Chem. A **13**, 35389 (2025).
[17] C. Ben Mahmoud, L. A. M. Rosset, J. R. Yates, and V. L. Deringer, J. Chem. Phys. **163**, 024107 (2025).
[18] M. Shakiba, A. B. Philips, J. Autschbach, and A. V. Akimov, J. Phys. Chem. Lett. **16**, 153 (2024).
[19] T. Charpentier, Faraday Discuss. **255**, 370 (2025).
[20] B. Schmiedmayer, J. W. Wolffs, G. A. de Wijs, A. P. M. Kentgens, J. Lahnsteiner, and G. Kresse, (2025).
[21] K. Wagle, D. A. Rehn, A. E. Mattsson, H. E. Mason, and M. W. Malone, Chem. Mater. **36**, 7162 (2024).
[22] A. F. Harper, T. Huss, S. S. Köcher, and C. Scheurer, Faraday Discuss. **255**, 411 (2025).
[23] M. Paulus, A. Paulus, P. Schleker, P. Jakes, R.-A. Eichel, P. Heitjans, and J. Granwehr, J. Magn. Reson. **303**, 57 (2019).
[24] A. Kuhn, V. Duppel, and B. V. Lotsch, Energy Environ. Sci. **6**, 3548 (2013).
[25] X. Liang, L. Wang, Y. Jiang, J. Wang, H. Luo, C. Liu, and J. Feng, Chem. Mater. **27**, 5503 (2015).

[26] A. Marko, K. Hogrefe, L. Schweiger, F. Stainer, J. Königsreiter, J. Spychala, J. Schwaiger, P. Heitjans, B. Gadermaier, and H. M. R. Wilkening, J. Am. Chem. Soc. **147** (2025), 10.1021/jacs.5c10283, aSAP.
[27] N. Kamaya, K. Homma, Y. Yamakawa, M. Hirayama, R. Kanno, M. Yonemura, T. Kamiyama, Y. Kato, S. Hama, K. Kawamoto, and A. Mitsui, Nat. Mater. **10**, 682 (2011).
[28] G. Materzanini, L. Kahle, A. Marcolongo, and N. Marzari, Phys. Rev. Mater. **5**, 035408 (2021).
[29] S. R. Xie, M. Rupp, and R. G. Hennig, npj Comput. Mater. **9**, 162 (2023).
[30] A. Grisafi, D. M. Wilkins, G. Csányi, and M. Ceriotti, Phys. Rev. Lett. **120**, 036002 (2018).
[31] A. P. Thompson, H. M. Aktulga, R. Berger, D. S. Bolintineanu, W. M. Brown, P. S. Crozier, P. J. in 't Veld, A. Kohlmeyer, S. G. Moore, T. D. Nguyen, R. Shan, M. J. Stevens, J. Tranchida, C. Trott, and S. J. Plimpton, Comput. Phys. Commun. **271**, 108171 (2022).
[32] D. J. Evans and B. L. Holian, J. Chem. Phys. **83**, 4069 (1985).
[33] J. Cheng, J. Luo, and K. Yang, Comput. Mater. Sci. **155**, 92 (2018).
[34] S. P. Ong, W. D. Richards, A. Jain, G. Hautier, M. Kocher, S. Cholia, D. Gunter, V. L. Chevrier, K. A. Persson, and G. Ceder, Comput. Mater. Sci. **68**, 314 (2013).
[35] S. Stegmaier, R. Schierholz, I. Povstugar, J. Barthel, S. P. Rittmeyer, S. Yu, S. Wengert, S. Rostami, H. Kungl, K. Reuter, R.-A. Eichel, and C. Scheurer, Adv. Energy Mater. **11**, 2100707 (2021).
[36] M. H. Levitt, *Spin Dynamics: Basics of Nuclear Magnetic Resonance*, 2nd ed. (John Wiley & Sons, 2008).
[37] A. Jerschow, Prog. Nucl. Magn. Reson. Spectrosc. **46**, 63 (2005).
[38] R. K. Harris, E. D. Becker, S. M. Cabral De Menezes, P. Granger, R. E. Hoffman, and K. W. Zilm, Pure Appl. Chem. **80**, 59 (2008).
[39] J. Granwehr and P. J. Roberts, J. Chem. Theory Comput. **8**, 3473 (2012).
[40] R. L. Parker and Y.-Q. Song, J. Magn. Reson. **174**, 314 (2005).
[41] P. Fantazzini, F. Galassi, V. Bortolotti, R. J. S. Brown, and F. Vittur, New J. Phys. **13**, 065007 (2011).
[42] H. Choi, I. Vinograd, C. Chaffey, and N. Curro, J. Magn. Reson. **331**, 107050 (2021).
[43] T. D. Davis and J. Granwehr, "Iltpy: Inverse laplace transform in python," Available at https://pypi.org/project/ilt-py-lib/ (2025).
[44] Z.-H. Fu, X. Chen, N. Yao, X. Shen, X.-X. Ma, S. Feng, S. Wang, R. Zhang, L. Zhang, and Q. Zhang, J. Energy Chem. **70**, 59 (2022).
[45] G. Winter and R. Gómez-Bombarelli, J. Phys. Energy **5**, 024004 (2023).
[46] K. Hogrefe, N. Minafra, W. G. Zeier, and H. M. R. Wilkening, J. Phys. Chem. C **125**, 2306 (2021).
[47] S. G. Bishop and P. J. Bray, J. Chem. Phys. **48**, 1709 (1968).
[48] B. Schmiedmayer, J. W. Wolffs, G. A. de Wijs, A. P. M. Kentgens, J. Lahnsteiner, and G. Kresse, e-print arXiv:2507.19435 (2025).
[49] P. Berman, O. Levi, Y. Parmet, M. Saunders, and Z. Wiesman, Concepts Magn. Reson., Part A **42**, 72 (2013).
[50] L. Schweiger, K. Hogrefe, B. Gadermaier, J. L. M. Rupp, and H. M. R. Wilkening, J. Am. Chem. Soc. **144**, 9597 (2022).
[51] K. Miwa and R. Asahi, Solid State Ionics **361**, 115567 (2021).
[52] X. He, Y. Zhu, and Y. Mo, Nat. Commun. **8**, 15893 (2017).
[53] T. Huss and F. Civaia, (2025), https://doi.org/10.17617/3.V4NSYB.